

國立臺灣大學理學院天文物理所

博士論文

Department of Computer Science and Information Engineering

College of Electrical Engineering and Computer Science

National Taiwan University

Doctoral Thesis

新的保守量與原始量的轉換法於狹義相對論性流體力  
學並使用高速圖形顯示卡於自適性網格

An adaptive mesh, GPU-accelerated, and error minimized  
special relativistic hydrodynamics code

曾柏勳

Po-Hsun Tseng

指導教授：闕志鴻博士

Advisor: Tzihong Chiueh, Ph.D.

中華民國 111 年 6 月

June, 2022



# 國立臺灣大學博士學位論文

## 口試委員會審定書

新的保守量與原始量的轉換法於狹義相對論性流  
體力學並使用高速圖形顯示卡於自適性網格

An adaptive mesh, GPU-accelerated, and error  
minimized special relativistic hydrodynamics code

本論文係曾柏勳君 (D05244001) 在國立臺灣大學天文物理所  
完成之博士學位論文，於民國 111 年 6 月 28 日承下列考試委員審  
查通過及口試及格，特此證明

口試委員：

<hr/>	
<hr/>	<hr/>
<hr/>	<hr/>
<hr/>	<hr/>
<hr/>	<hr/>

所 長：

<hr/>
-------



# 誌謝

感謝...



# Acknowledgements

I'm glad to thank. . .





# 摘要

本論文提出了一影像中使用者感興趣區域 (region of interest) 偵測之資料集 (benchmark)。使用者感興趣區域偵測在許多應用中極為有用，過去雖然有許多使用者感興趣區域之自動偵測演算法被提出，然而由於缺乏公開資料集，這些方法往往只測試了各自的小量資料而難以互相比較。從其它領域可以發現，基於公開資料集的可重製實驗與該領域突飛猛進密切相關，因此本論文填補了此領域之不足，我們提出名為「Photoshoot」的遊戲來蒐集人們對於感興趣區域的標記，並以這些標記來建立資料集。透過這個遊戲，我們已蒐集大量使用者對於感興趣區域的標記，並結合這些資料成為使用者感興趣區域模型。我們利用這些模型來量化評估五個使用者感興趣區域偵測演算法，此資料集也可更進一步作為基於學習理論演算法的測試資料，因此使基於學習理論的偵測演算法成為可能。

**關鍵字：** 相對論性流體演算法、費米氣泡、義羅西塔氣泡



# Abstract

We present a new special relativistic hydrodynamics (SRHD) code capable of handling coexisting ultra-relativistically hot and non-relativistically cold gases. We achieve this by designing a new algorithm for conversion between primitive and conserved variables in the SRHD solver, which incorporates a realistic ideal-gas equation of state covering both the relativistic and non-relativistic regimes. The code can handle problems involving a Lorentz factor as high as  $10^6$  and optimally avoid the catastrophic cancellation. In addition, we have integrated this new SRHD solver into the code `GAMER` (<https://github.com/gamer-project/gamer>) to support adaptive mesh refinement and hybrid OpenMP/MPI/GPU parallelization. It achieves a peak performance of  $7 \times 10^7$  cell updates per second on a single Tesla P100 GPU and scales well to 2048 GPUs. We apply this code to two interesting astrophysical applications: (a) an asymmetric explosion source on the relativistic blast wave and (b) the flow acceleration and limb-brightening of relativistic jets.

**Keywords:** relativistic jets, numerical method



# Contents

口試委員會審定書	iii
誌謝	v
Acknowledgements	vii
摘要	ix
Abstract	xi
1 Introduction	1
Part I	3
2 Special relativistic hydrodynamics	5
2.1 Relativistic hydrodynamics . . . . .	5
2.2 Equations of state . . . . .	7
2.3 Conversion between primitive and conserved variables . . . . .	10
3 Numerical methods	15
3.1 A GAMER Primer . . . . .	15
3.2 Flexible Time-step . . . . .	16
3.3 Handling unphysical results . . . . .	18
4 Test problems	21
4.1 Convergence test for sinusoidal waves . . . . .	21

4.2	1-D relativistic Riemann problems . . . . .	22
4.3	Ultra-relativistic limit . . . . .	23
4.4	Mixed limits . . . . .	25
4.5	Multi-dimensional grid effects for high- $\mathcal{M}$ flows . . . . .	27
<b>Bibliography</b>		<b>31</b>

# List of Figures

- 2.1 The effective adiabatic index  $\Gamma$  (top left), the reduced enthalpy  $\tilde{h}/c^2 := h/c^2 - 1$  (top right) as a function of temperature. Bottom panels show that Equation (2.10) approaches Equation (2.9) in both high- and low- $T$  limits, where the maximum relative errors  $1 - \Gamma_{\text{TM}}/\Gamma_{\text{exact}}$  and  $1 - \tilde{h}_{\text{TM}}/\tilde{h}_{\text{exact}}$ , are only 1.9 and 2.0 per cent, respectively. . . . . 9
- 2.2 Numerical errors of the conversion from conserved to primitive variables as a function of  $\mathcal{M}$  and  $k_B T/mc^2$ . The top and middle panel show the errors of the new and original schemes estimated by Equation (2.20) and Equation (2.21), respectively. The bottom panel shows the ratio of Equation (2.21) to Equation (2.20). ?? in Appendix ?? provides numerical evidences showing a remarkable consistency with the predicted values at  $k_B T/mc^2 = 10^{-8}$  (blue dashed-dotted line). . . . . 13

4.1 Riemann problem in the UR limit with a head-on collision of two identical gases with  $\beta\gamma = 10^6$  and  $k_B T/mc^2 = 10^5$  at  $t = 1.0$ . The left column shows the entire simulation domain, while the right column shows the zoom-in image of the post-shock region. From top to bottom: pressure, proper mass density, four-velocity, and temperature. Note that we plot the Mach number in the zoom-in image (right column) of four-velocity so as to readily compare the amplitude of velocity oscillation with sound speed. The new scheme (blue circles) fully agrees with the original scheme (olive crosses) not only on the large-scale profiles but also on the small-scale errors, meaning that the new scheme (blue circles) does not sacrifice (or improve) the numerical accuracy in the UR limit for that in the NR limit. . 24

4.2 Riemann problem in the mixed UR and NR limits at  $t = 80$ . The second row in Table 4.1 shows the initial condition. Clock-wise from top-left: pressure, 4-velocity, temperature, and proper mass density. We find not only that the shock front at  $x = 26$  is well resolved by 3–4 cells but also that the new scheme (red crosses) agrees well with the exact solution of the TM EoS (yellow lines), as shown in all insets. The L1 error of the density profile from the original scheme (black circles) is 23 per cent within the region between the head of rarefaction wave and initial discontinuity (i.e.  $2.67 \times 10^{-2} < x < 5 \times 10^{-2}$ ), consistent with the 20 per cent error estimated by Equation (4.2) with  $k_B T/mc^2 = 8 \times 10^{-6}$ . However, in the region  $5 \times 10^{-2} < x < 0.3$  swept by the right-traveling contact discontinuity, errors of the original scheme are much larger than the estimate, which requires further investigation. The TM profiles match well with both the  $\Gamma = 5/3$  profiles (blue dashed lines) in the NR region ( $x < 0.21$ ) and the  $\Gamma = 4/3$  profiles (green dashed lines) in the UR region ( $x > 0.27$ ). . . . . 26



- 4.3 Ultra-relativistic flows propagating along different spatial directions with respect to the grids. In all subfigures (a)–(d), the left and right columns are the longitudinal and transverse slices, respectively. Longitudinal slices are taken through the flow source while the transverse slices are taken through the label ‘A’. The flow diameter is resolved by 28 cells in (a) and (b) and by 56 cells in (c) and (d). The flow has an extremely high Mach number ( $\mathcal{M} \sim 10^6$ ) leaving any instability short of time to develop, and one expects a smooth flow-ambient interface. However, the fuzzy-looking cross-sections in the transverse slices of the oblique flow (right columns in (b) and (d)) suggest that the high-speed flow induces false instability when the flow travels obliquely across Cartesian grids. Increasing the spatial and temporal resolution does not help the numerical solution of an oblique flow to converge to that of a parallel flow. . . . . 29
- 4.4 Close-up view of the rectangular region in Figure 4.3(c) with longitudinal (first column from the left) and transverse (other columns) slices passing through ‘B’ and ‘C’, respectively. Compared with Figure 4.3(c), it clearly shows that the finger pattern consists of 2-D flat sheets along the flow. . . 30



# List of Tables

4.1 The left and right initial states of the Riemann problems in Section 4.2.

We denote the left/right states by the subscript  $L/R$ . . . . . 23



# Chapter 1

## Introduction

Many high energy astrophysical problems involve relativistic flows. The problems include, for example, collimated jets in active galactic nuclei (AGN) (Chiueh et al. 1991; Li et al. 1992; Blandford et al. 2019), collapsar models of long-duration gamma-ray bursts [Woosley, 1993], magnetized relativistic winds and nebulae from pulsars (Kennel and Coroniti 1984a; Kennel and Coroniti 1984b; Chiueh 1989; Chiueh et al. 1998), and mildly relativistic wide-angle outflows in neutron star mergers (Mooley et al. 2018a; Mooley et al. 2018b; Ghirlanda et al. 2019; Fong et al. 2019). The full scope of these problems generally involves substantial temperature changes between jets (winds) and ambient gases. For this reason, the pioneering works of Taub [1948], Mathews [1971], and Mignone et al. [2005] suggested Taub-Mathews equation of state (TM EoS) that approximates the exact EoS [Synge, 1957] for ultra-relativistically hot (high- $T$  hereafter) gases coexisting with non-relativistically cold (low- $T$  hereafter) gases.

In addition, Noble et al. [2006] first compared the accuracy of several schemes for recovering primitive variables in the Riemann problems by means of self-checking tests (see Appendix ?? for details). Mignone and McKinney [2007] further proposed an inversion scheme for an arbitrary EoS and suggested that directly evolving the reduced energy density (i.e. the energy density subtracting the rest mass energy density from the total energy density) can avoid catastrophic cancellation in the non-relativistic limit. However, very few studies have systematically investigated how serious the catastrophic cancellation bears upon simulation results. This is partially due to the lack of exact

solutions with which numerical results can be compared.

In this paper, we propose a new numerical scheme for conversion between primitive and conserved variables in the presence of both high- $T$  and low- $T$  gases. The new scheme is carefully tailored to avoid catastrophic cancellation. To verify its accuracy, we numerically derive the exact solutions of two relativistic Riemann problems with the TM EoS and compare with the simulation results. It demonstrates that our new special relativistic hydrodynamics (SRHD) code can minimize numerical errors compared with conventional methods.

We have integrated this new SRHD solver into the code `GAMER` (Schive et al. 2010; Schive et al. 2018) to facilitate GPU acceleration and adaptive mesh refinement (AMR). This new code, `GAMER-SR`, yields good weak and strong scalings using up to 2048 GPUs on `Piz-Daint`, the supercomputer at the Swiss National Supercomputing Centre (CSCS). Finally, we present two astrophysical applications, an asymmetric explosion and self-accelerating jets, to demonstrate the capability of this new code in extreme conditions. All simulation data are analysed and visualized using the package `yt` [Turk et al., 2011].

This paper is organized as follows. We introduce the equation of state and our new scheme for conversion between primitive and conserved variables in Section ???. In Section ??, we describe numerical methods, including the AMR structure, GPU acceleration, flexible time-steps, and correction of unphysical results. In Sections ?? and ??, we conduct numerical experiments to demonstrate the accuracy in both the non-relativistic (NR) and ultra-relativistic (UR) limits, the performance scalability, as well as the limitation of `GAMER-SR`. Finally, we present two astrophysical applications in Section ?? and draw the conclusion in Section ??.

Note that the speed of light and the Boltzmann constant are hard-coded to 1 in `GAMER-SR`. However, these physical constants are retained in this paper, except in Appendices, for dimensional consistency.

# **Part I**

## **Special relativistic hydrodynamics**





# Chapter 2

## Special relativistic hydrodynamics

### 2.1 Relativistic hydrodynamics

Mass and energy-momentum conservation laws of a special relativistic ideal fluid follow

$$\partial_\nu (\rho U^\nu) = 0, \quad (2.1a)$$

$$\partial_\nu T^{\mu\nu} = 0, \quad (2.1b)$$

where

$$T^{\mu\nu} = \rho h U^\mu U^\nu / c^2 + p \eta^{\mu\nu}. \quad (2.2)$$

$\rho$  and  $p$  are the proper mass density and the pressure,  $U^\mu$  the four-velocity,  $\eta^{\mu\nu}$  the metric tensor of Minkowski space, and  $c$  the speed of light.  $h$  is the specific enthalpy, related to the specific thermal energy  $\epsilon$  by

$$h = c^2 + \epsilon + \frac{p}{\rho}. \quad (2.3)$$

An equation of state,  $h(\rho, p)$ , is required to close Equation (2.1) and will be discussed in Section 2.2. Throughout this paper, lower-case Greek indices run from 0 to 3, Latin ones from 1 to 3, and the Einstein summation convention is used, except when stated otherwise.

Equation (2.1) can be rewritten into a convenient conservative form for numerical

integration:

$$\partial_t D + \partial_j (DU^j / \gamma) = 0, \quad (2.4a)$$

$$\partial_t M^i + \partial_j (M^i U^j / \gamma + p \delta^{ij}) = 0, \quad (2.4b)$$

$$\partial_t E + \partial_j (M^j c^2) = 0, \quad (2.4c)$$

where  $\gamma$  is the Lorentz factor, and  $\delta^{ij}$  is the Kronecker delta notation.

The five conserved quantities  $D$ ,  $M^i$ , and  $E$  are the mass density, the momentum densities, and the total energy density, respectively. All conserved variables are related to primitive variables  $(\rho, U^i, p)$  through

$$D = \rho \gamma, \quad (2.5a)$$

$$M^i = D h U^i / c^2, \quad (2.5b)$$

$$E = D h \gamma - p. \quad (2.5c)$$

Nevertheless, Mignone and McKinney [2007] suggest evolving the reduced energy density,

$$\tilde{E} := E - D c^2, \quad (2.6)$$

instead of the total energy density; otherwise, extraction of a tiny thermal energy for a cold gas from the total energy will lead to catastrophic cancellation. An intuitive approach is to subtract Equation (2.4a) from Equation (2.4c) so that we can obtain a new energy equation. However, the new energy flux,  $(M^j - DU^j / \gamma) c^2$ , also suffers from catastrophic cancellation in the NR limit. An appropriate new energy flux avoiding such a problem is  $(\tilde{E} + p) U^j / \gamma$ , which is mathematically equivalent to  $(M^j - DU^j / \gamma) c^2$ . The reduced energy equation for numerical integration can thus be cast into

$$\partial_t \tilde{E} + \partial_j [(\tilde{E} + p) U^j / \gamma] = 0, \quad (2.7)$$

which is to replace Equation (2.4c).

Moreover, solving the Lorentz factor  $\gamma$  as three-velocity ( $v = \sqrt{v^i v_i}$ ) approaches  $c$  can seriously suffer from catastrophic cancellation when using  $\gamma = 1/\sqrt{1 - v^i v_i/c^2}$ . Therefore, we explicitly adopt four-velocities ( $U^i$ ) instead of three-velocity ( $v^i$ ) for numerical computations and solve the Lorentz factor in terms of four-velocities as

$$\gamma = \sqrt{1 + U^i U_i/c^2}, \quad (2.8)$$

by which significant digits in  $\gamma$  can be kept when  $\gamma \gg 1$ .

In addition, unlike the three-velocity bounded by  $c$ , four-velocity  $U^i$  has no upper limit and therefore can greatly reduce the risk of having  $v > c$  due to numerical errors.

## 2.2 Equations of state

GAMER-SR supports two kinds of EoS, the Taub-Mathews EoS (TM; Taub 1948, Mathews 1971, Mignone et al. 2005) and the polytropic EoS with a constant ratio of specific heats  $\Gamma$ . Assuming an ideal fluid in local thermal equilibrium and obeying the non-degenerate Maxwell-Jüttner statistics [Jüttner, 1911], the exact EoS [Synge, 1957] derived from the kinetic theory of relativistic gases is given by

$$\frac{h_{\text{exact}}}{c^2} = \frac{K_3 (mc^2/k_B T)}{K_2 (mc^2/k_B T)}, \quad (2.9)$$

where  $k_B$  and  $T$  are the Boltzmann constant and temperature, respectively, and  $K_n$  the  $n$ -th order modified Bessel function of the second kind. However, direct use of Equation (2.9) is computationally inefficient because the evaluation of Bessel function is numerically expensive.

Alternatively, the TM EoS is an approximation of Equation (2.9) and given by

$$\frac{h_{\text{TM}}}{c^2} = 2.5 \left( \frac{k_B T}{mc^2} \right) + \sqrt{2.25 \left( \frac{k_B T}{mc^2} \right)^2 + 1}. \quad (2.10)$$

The effective  $\Gamma$  can be found by equating Equation (2.9) or Equation (2.10) to the

polytropic EoS,

$$\frac{h_\Gamma}{c^2} = 1 + \frac{\Gamma}{\Gamma - 1} \left( \frac{k_B T}{mc^2} \right), \quad (2.11)$$

and solving  $\Gamma$  for the exact or TM EoS, respectively. As depicted in Figure 2.1, the maximum relative errors  $1 - \Gamma_{\text{TM}}/\Gamma_{\text{exact}}$  and  $1 - \tilde{h}_{\text{TM}}/\tilde{h}_{\text{exact}}$  are found to be only 1.9 and 2.0 per cent, respectively. In addition, Equation (2.10) approaches Equation (2.9) in both high- and low- $T$  limits. Detailed comparisons between Equation (2.9) and Equation (2.10) have been presented previously (Mignone et al. 2005; Ryu et al. 2006; Mignone and McKinney 2007) and we do not repeat here.

On the other hand, the polytropic EoS has the advantage of simplicity and therefore has been used in many SRHD codes, such as FLASH [Fryxell et al., 2000], CAFE [Lora-Clavijo et al., 2015], and XTROEM-FV [Núñez-de la Rosa and Munz, 2016]. However, the polytropic EoS cannot handle the case where relativistic gases and non-relativistic gases coexist, primarily because the ratio of specific heats depends sensitively on temperature when  $k_B T \sim mc^2$  (see the upper left panel in Figure 2.1). Moreover, the polytropic EoS with a non-relativistic  $\Gamma = 5/3$  and a relativistic  $\Gamma = 4/3$  does not satisfy the Taub's fundamental inequality for ideal gases [Taub, 1948]

$$\left[ \frac{h}{c^2} - \left( \frac{k_B T}{mc^2} \right) \right] \left[ \frac{h}{c^2} - 4 \left( \frac{k_B T}{mc^2} \right) \right] \geq 1, \quad (2.12)$$

implying that  $\Gamma$  must lie between  $4/3$  and  $5/3$  for any positive and finite value of temperature. Although the polytropic EoS is physically incorrect, we still reserve this feature in GAMER-SR for fast computation of a pure non-relativistic or relativistic gas.

The other two important quantities are the Mach number ( $\mathcal{M}$ ) and the sound speed ( $c_s$ ), given by

$$\mathcal{M} = \frac{\sqrt{U^i U_i}}{U_s}, \quad (2.13)$$

and

$$\frac{c_s}{c} = \sqrt{\frac{k_B T/mc^2}{3h/c^2} \left( \frac{5h/c^2 - 8k_B T/mc^2}{h/c^2 - k_B T/mc^2} \right)}, \quad (2.14)$$

for the TM EoS, where  $U_s = c_s/\sqrt{1 - (c_s/c)^2}$ . The sound speed approaches  $c/\sqrt{3}$  at

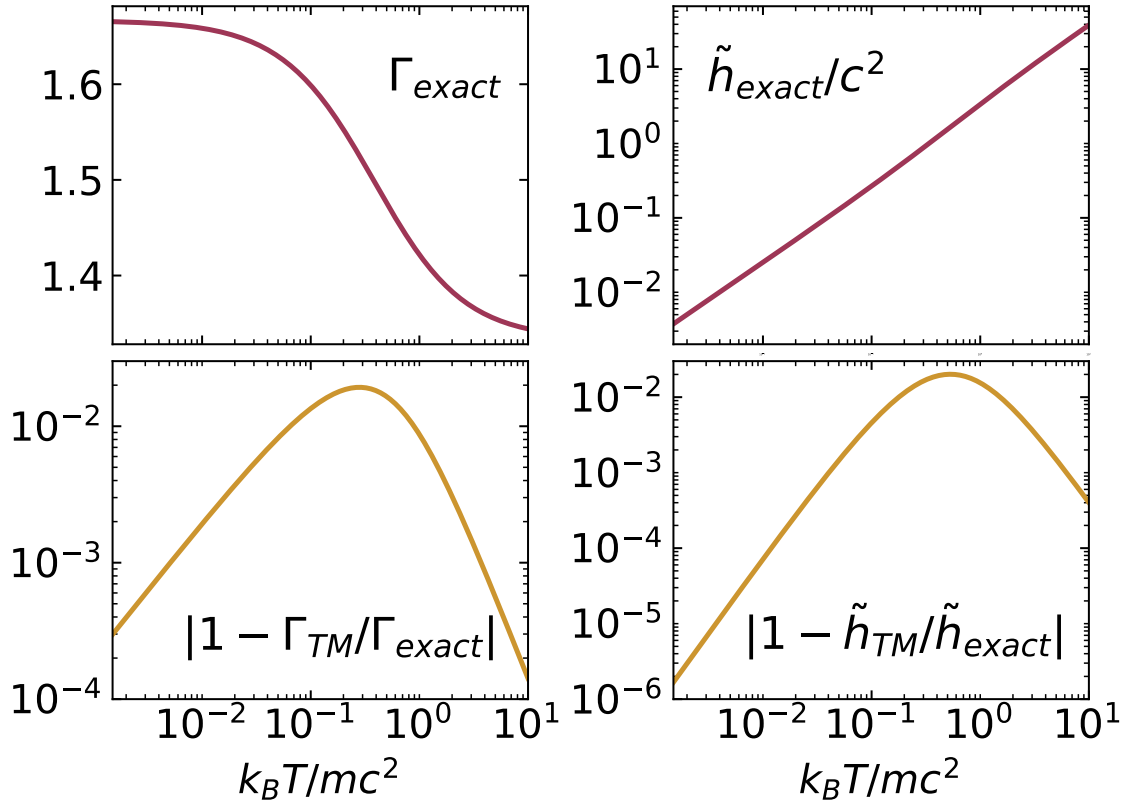


Figure 2.1: The effective adiabatic index  $\Gamma$  (top left), the reduced enthalpy  $\tilde{h}/c^2 := h/c^2 - 1$  (top right) as a function of temperature. Bottom panels show that Equation (2.10) approaches Equation (2.9) in both high- and low- $T$  limits, where the maximum relative errors  $1 - \Gamma_{TM}/\Gamma_{exact}$  and  $1 - \tilde{h}_{TM}/\tilde{h}_{exact}$ , are only 1.9 and 2.0 per cent, respectively.

ultra-relativistic temperature and will be used in the Riemann solver.

## 2.3 Conversion between primitive and conserved variables

In standard Riemann-type numerical schemes, conversion between conserved and primitive variables is a common procedure for data reconstructions and flux computations. For non-relativistic hydrodynamics, this conversion can be carried out in a straightforward and analytical manner. However, designing an accurate and efficient conversion algorithm for a relativistic problem in the presence of NR gases, which involves root-finding, is challenging. This is because catastrophic cancellations may arise in the non-relativistic gas.

Here we propose a new conversion scheme to solve this problem based on the TM EoS. The reduced energy density (Equation 2.6) and the momentum density (Equation 2.5b) satisfy the relation

$$\begin{aligned} & \left( \frac{\tilde{E}}{Dc^2} \right)^2 + 2 \left( \frac{\tilde{E}}{Dc^2} \right) - \left( \frac{\mathbf{M}}{Dc} \right)^2 \\ &= \frac{\tilde{h}^2}{c^4} + \frac{2\tilde{h}}{c^2} - 2 \left( \frac{k_B T}{mc^2} \right) \left( \frac{\tilde{h}}{c^2} + 1 \right) + \frac{(k_B T/mc^2)^2 (\tilde{h} + c^2)^2}{(\tilde{h} + c^2)^2 + \left( \frac{Mc}{D} \right)^2} \\ &:= f(\tilde{h}), \end{aligned} \quad (2.15)$$

where  $f$  is positive definite,  $\tilde{h} := h - c^2$  is the reduced enthalpy, and the temperature  $k_B T/mc^2$  is related to  $\tilde{h}$  by inverting Equation (2.10):

$$\frac{k_B T}{mc^2} = \frac{2(\tilde{h}/c^2)^2 + 4(\tilde{h}/c^2)}{5(\tilde{h}/c^2) + 5 + \sqrt{9(\tilde{h}/c^2)^2 + 18(\tilde{h}/c^2) + 25}}. \quad (2.16)$$

The conserved variables  $\tilde{E}$ ,  $M^j$ , and  $D$  on the left-hand side are known quantities updated at every time step, from which one can solve for  $\tilde{h}$ .

We adopt  $\tilde{h} = h - c^2$  instead of  $h$  as the root because the latter is dominated by rest mass energy density in the low- $T$  limit and thus will suffer from catastrophic cancellation when numerically extracting temperature from trailing digits.

Equation (2.15) is suitable for the Newton-Raphson iteration method as it is a monotonically increasing function of  $\tilde{h}$ . That is, Equation (2.15) has no zero derivative of  $\tilde{h}$  that might otherwise lead to a divergence of the iterative procedure. The Newton-Raphson method requires an initial guess of  $\tilde{h}$  and the derivative of Equation (2.15) for iteration, both of which are presented in Appendix ?? . We adopt the convergence criterion  $1 - \tilde{h}_i/\tilde{h}_{i+1} \leq \epsilon_{\text{machine}}$ , where  $\tilde{h}_i$  is the approximate root at the  $i$ th iteration and  $\epsilon_{\text{machine}}$  is the machine precision ( $10^{-7}$  and  $10^{-16}$  for single and double precision, respectively).

After obtaining  $\tilde{h}$ , we substitute it into Equation (2.5b) to get four-velocity:

$$U^i = \frac{M^i c^2}{D(c^2 + \tilde{h})}. \quad (2.17)$$

Next, we compute the Lorentz factor and proper mass density from Equation (2.8) and Equation (2.5a) and then use Equation (2.16) to obtain temperature. Finally, the pressure is given by

$$p = \rho c^2 \left( \frac{k_B T}{mc^2} \right). \quad (2.18)$$

Justifying the superiority of our new conversion scheme using  $\tilde{E}$ , we estimate the relative error of computing  $a - b$  by [Higham, 2002]

$$\frac{|a| + |b|}{|a - b|} \epsilon_{\text{machine}}. \quad (2.19)$$

Thus, the error of the new conversion scheme can be estimated by substituting  $\left[ (\tilde{E}/Dc^2)^2 + 2(\tilde{E}/Dc^2) \right]$  and  $(\mathbf{M}/Dc)^2$  for  $a$  and  $b$ , respectively, in Equation (2.19). The error in terms of primitive variables reads

$$\begin{aligned} & \left[ \frac{\gamma^2 (\tilde{h} + 1)^2 (1 + \beta^2) + \frac{T^2}{\gamma^2} - 2(\tilde{h} + 1)T - 1}{(\tilde{h} + 1)^2 + \frac{T^2}{\gamma^2} - 2(\tilde{h} + 1)T - 1} \right] \epsilon_{\text{machine}} \\ & \approx (1 + \mathcal{M}^2) \epsilon_{\text{machine}}, \end{aligned} \quad (2.20)$$

where  $\beta = \sqrt{v^i v_i}/c$ . The approximate equality in Equation (2.20) holds for all finite temperature.

According to Equation (2.13) and Equation (2.20), we can decide whether to adopt single or double precision before simulations. Taking ultra-relativistic pulsar wind ( $\mathcal{M}_{\text{wind}} \approx 10^6$ ) as an example, we must use double precision to suppress the error to  $10^{-4}$ . But for mild-relativistic AGN jets ( $\mathcal{M}_{\text{jet}} < 10$ ), single precision is sufficient to reduce the error to  $10^{-5}$ .

For the original scheme using the total energy density  $E$  instead of  $\tilde{E}$ , a similar error estimation can be performed by replacing  $\tilde{E}$  with  $E - Dc^2$  on the left-hand side of Equation (2.15), which gives

$$\left[ \frac{2\gamma^2 (\tilde{h} + 1)^2 + \frac{T^2}{\gamma^2} - 2(\tilde{h} + 1)T + (\tilde{h} + 1)^2 + 1}{(\tilde{h} + 2)\tilde{h} + \frac{T^2}{\gamma^2} - 2(\tilde{h} + 1)T} \right] \epsilon_{\text{machine}}. \quad (2.21)$$

Figure 2.2 shows the contour plots of Equation (2.20) for the new scheme (top panel) and Equation (2.21) for the original scheme (middle panel) as a function of  $\mathcal{M}$  and temperature. The bottom panel shows the ratio of Equation (2.21) to Equation (2.20). It demonstrates the advantage of using  $\tilde{E}$ . The top panel shows that using  $\tilde{E}$  in the conversion scheme is almost error-free when dealing with subsonic flows at any finite temperature, including the low- $T$  limit. In supersonic flows, the numerical errors proportional to  $\mathcal{M}^2$  are common and caused by finite digits of floating numbers. In comparison, the middle panel shows the error using  $E$ , which severely suffers from catastrophic cancellation in the low- $T$  limit even when  $\mathcal{M} \ll 1$ . See also ?? in Appendix ??.

On the other hand, conversion from primitive to conserved variables is also needed in the Riemann solver. This procedure involves straightforward substitution without the need of root-finding. We use

$$\frac{\tilde{h}}{c^2} = 2.5 \left( \frac{k_B T}{mc^2} \right) + \frac{2.25 (k_B T / mc^2)^2}{1 + \sqrt{2.25 (k_B T / mc^2)^2 + 1}}, \quad (2.22)$$

and

$$\frac{\tilde{E}}{Dc^2} = \frac{\left( \frac{\mathbf{M}}{Dc} \right)^2 + f(\tilde{h})}{1 + \sqrt{1 + \left( \frac{\mathbf{M}}{Dc} \right)^2 + f(\tilde{h})}}, \quad (2.23)$$

to compute  $\tilde{h}$  and  $\tilde{E}$ , where  $f(\tilde{h})$  can be computed from Equation (2.15) with known  $\mathbf{M}/Dc$ . Note that Equation (2.22) and Equation (2.23), following directly from Equation (2.10) and Equation (2.15) without any approximation, are written in a form without any subtraction to avoid catastrophic cancellation. In contrast, using Equation (2.5c) and Equation (2.6) to compute the reduced energy density  $\tilde{E}$  can suffer from catastrophic cancellation in the NR limit.

We close this section by providing a flowchart of the new conversion scheme in ?? in Appendix ?? and by summarizing the equations actually solved by GAMER-SR. Other mathematically equivalent forms are unrecommended as they may suffer from catastrophic cancellation in the UR or NR limit.

- Evolution equations: Equation (2.4a, 2.4b, 2.7).



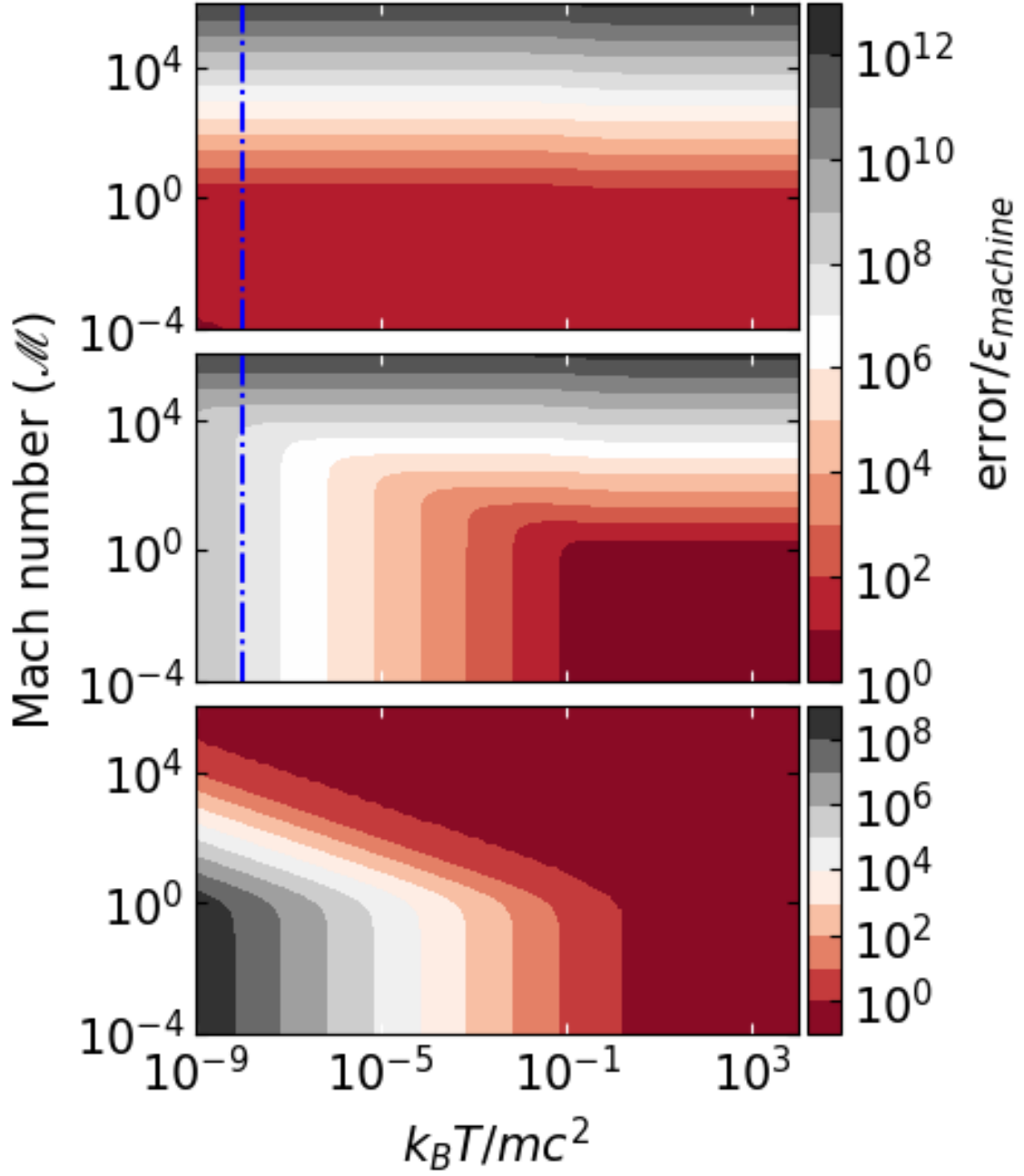


Figure 2.2: Numerical errors of the conversion from conserved to primitive variables as a function of  $\mathcal{M}$  and  $k_B T / m c^2$ . The top and middle panel show the errors of the new and original schemes estimated by Equation (2.20) and Equation (2.21), respectively. The bottom panel shows the ratio of Equation (2.21) to Equation (2.20). ?? in Appendix ?? provides numerical evidences showing a remarkable consistency with the predicted values at  $k_B T / m c^2 = 10^{-8}$  (blue dashed-dotted line).

- Lorentz factor: Equation (2.8).
- Four-velocities: Equation (2.17).
- Temperature: Equation (2.16).
- Pressure: Equation (2.18).
- Reduced enthalpy: Equation (2.22).
- Reduced energy density: Equation (2.23).

# Chapter 3

## Numerical methods

### 3.1 A GAMER Primer

Due to the flexibility and extensibility of GAMER (Schive et al. 2010; Schive et al. 2018), the SRHD module directly inherits the AMR structure and the MPI/OpenMP/GPU parallelization framework of hydrodynamics, and therefore we only provide a summary here. We define the base grid resolution as level-0 and the  $\ell$ th refinement as level- $\ell$ , where level- $\ell$  has a spatial resolution  $2^\ell$  times higher than that of the base level. Data in GAMER are always decomposed into patches, each of which consists of  $8^3$  cells, and the AMR implementation is realized by constructing a hierarchy of patches in an octree structure. According to user-defined refinement criteria, we can create or remove fine patches under the proper-nesting constraint.

In addition to the refinement criteria provided by the hydrodynamics module, we also implement two refinement criteria for SRHD: the gradient of the Lorentz factor and the magnitude of  $|\mathbf{M}|/D$ . The former aims to capture the thin and high- $\gamma$  shell in the Sedov-Taylor blast wave, while the latter ensures that the spine region in an over-pressured jet (cf. ??) can be fully resolved. For all refinement criteria, the refinement thresholds on different levels can be set independently as run-time parameters.

We port the routines involving massive floating-point operations to GPUs such as the SRHD solvers and time-step calculations. On the other hand, we use CPUs to perform ghost-zone interpolation and patch refinement. As a result, we recommend using the

refinement criteria only involving conserved variable for better performance because conserved variables are readily available from memory. By contrast, primitive variables can only be obtained by root-finding iteration, which is computationally expensive.

For enhancing software portability and reusability, GAMER not only supports both CPU-only and GPU modes but also allows the same physics modules to be shared by both CPU and GPU computations. Specifically, in the CPU-only mode, we compute different grid patches in the same MPI process in parallel with OpenMP. In the GPU mode, we replace these OpenMP parallel clauses with CUDA thread blocks and then use threads within the same thread block to update all cells within the same grid patch. This scheme maximizes the reuse of physics routines, avoids redundant code development and maintenance, and significantly lowers the barrier of code extension, especially for developers not acquainted with GPU programming. We have utilized this CPU/GPU integration infrastructure in the SRHD implementation.

GAMER-SR supports the MUSCL-Hancock [Toro, 2011] and VL (Falle 1991; van Leer 2006) schemes for numerical integrations and both piece-wise linear method (PLM; van Leer 1979) and piecewise parabolic method (PPM; Woodward and Colella 1984) for data reconstruction. For the Riemann solver, it supports both relativistic HLLC and HLLE solvers (Mignone and Bodo 2005; Mignone and Bodo 2006), which have been adapted not only to be compatible with the TM EoS by using the corresponding sound speed, Equation (2.14), but also to evolve the reduced energy density (i.e. replacing  $E$  with  $\tilde{E} + Dc^2$ ).

## 3.2 Flexible Time-step

GAMER-SR provides two Courant-Friedrichs-Lewy (CFL) conditions for time-step determination. The first one is based on the local signal propagation speed,  $S_{\max}$ , which gives maximum allowed time-steps in a wide dynamical range. Thus, it can significantly improve performance when the maximum  $v/c$  is not close to unity. The other is based on the speed of light, where we simply replace  $S_{\max}$  by  $c$ . It gives the most conservative estimation of time-steps and is more time-consuming when the flow speed is far less than

$c$ , although it is simple to implement and requires less computation.

To calculate  $S_{\max}$ , we first define  $\hat{\mathbf{u}}_s$  to be a spatial unit vector in the direction of sound propagation, we then apply the Lorentz boost with velocity  $-\boldsymbol{\beta}$  to the four-velocity of sound speed  $(\gamma_s, U_s \hat{\mathbf{u}}_s)$  from local rest frame to laboratory frame. We finally obtain the four-velocity of signal that travels in laboratory frame as follows:

$$\left( \gamma\gamma_s + \gamma U_s (\boldsymbol{\beta} \cdot \hat{\mathbf{u}}_s), U_s \hat{\mathbf{u}}_s + (\gamma - 1) U_s (\hat{\boldsymbol{\beta}} \cdot \hat{\mathbf{u}}_s) \hat{\boldsymbol{\beta}} + \boldsymbol{\beta} \gamma \gamma_s \right), \quad (3.1)$$

where  $\gamma$  and  $\gamma_s$  are the Lorentz factor of flow and of sound speed.  $U_s$  is the four-velocity of sound speed defined by  $c_s/\sqrt{1-c_s^2}$ . Since the direction of the fastest signal propagation is in general parallel to flow velocity, we assume that both sound and flow propagate in the same direction (i.e.  $\hat{\mathbf{u}}_s = \hat{\boldsymbol{\beta}}$ ). The spatial components of Equation (3.1) then reduce to

$$(\beta\gamma\gamma_s + \gamma U_s) \hat{\boldsymbol{\beta}}. \quad (3.2)$$

Motivated by Equation (3.2), we simply choose  $U^i \gamma_s + \gamma U_s$  as the bound of each spatial component and sum over  $U^i \gamma_s + \gamma U_s$  for each spatial component to obtain

$$U_{\max} = \gamma_s (U_x + U_y + U_z) + 3\gamma U_s, \quad (3.3)$$

where  $U_{x/y/z}$  is the  $x/y/z$ -component of the four-velocities of flow.

Note that Equation (3.3) is essentially the addition of flow speed and sound speed in special relativity theory. Converting Equation (3.3) back to three-velocity

$$S_{\max} = U_{\max} / \sqrt{1 + (U_{\max}/c)^2}, \quad (3.4)$$

and substituting Equation (3.4) into the CFL condition, we finally obtain the flexible time-step based on the local signal propagation speed for SRHD:

$$\Delta t = C_{\text{CFL}} \left( \frac{\Delta h}{S_{\max}} \right), \quad (3.5)$$

where  $\Delta h$  is the cell spacing and  $C_{\text{CFL}}$  the safety factor with a typical value of  $\sim 0.5$  for MUSCL-Hancock and VL schemes.

Note that Equation (3.5) can be reduced to its non-relativistic counterpart,

$$\Delta t = C_{\text{CFL}} \left( \frac{\Delta h}{v_x + v_y + v_z + 3c_s} \right), \quad (3.6)$$

when  $\gamma \sim 1$  and to  $\Delta t = C_{\text{CFL}} \Delta h / c$  when  $\gamma \gg 1$ .

### 3.3 Handling unphysical results

Unphysical results, for example, negative pressure, negative density and superluminal motion, can stem from the failure of the following criterion:

$$\left( \frac{\tilde{E}}{Dc^2} \right)^2 + 2 \left( \frac{\tilde{E}}{Dc^2} \right) - \left( \frac{\mathbf{M}}{Dc} \right)^2 > \epsilon_{\text{machine}}, \quad (3.7)$$

where the left-hand side involves the numerically updated quantities and  $\epsilon_{\text{machine}}$  is the machine epsilon – typically,  $2 \times 10^{-16}$  for double precision and  $1 \times 10^{-7}$  for single precision.

The failure may take place in one of the following four steps:

#### (1) SRHD solver

SRHD solver is responsible for updating the conserved variables by a given time-step. If unphysical result occurs in a cell, we redo data reconstruction by reducing the original minmod coefficient by a factor of 0.75. If the failure still occurs, we further reduce the minmod coefficient repeatedly until Equation (3.7) passes or the reduced minmod coefficient vanishes. Note that interpolating with a vanished minmod coefficient is essentially equivalent to the piece-wise constant spatial reconstruction.

#### (2) Grid refinement

Unphysical results may occur during grid refinement when performing interpolations on parent patches. The remedy here is the same as that in the SRHD solver. We repeat the interpolation process with a reduced minmod coefficient on the conserved variables until Equation (3.7) passes or the minmod coefficient vanishes. A vanished minmod

coefficient is essentially equivalent to directly copying data from the parent patch without interpolation.

*(3) Ghost-zone interpolation*

To preserve conservation, where the volume-weighted average of child patch data are equal to its parent patch data, we normally fill the ghost zones of the patches on level  $\ell + 1$  by interpolating the conserved variables on level  $\ell$  when the ghost zones lie on level  $\ell$ . However, if unphysical results occur, we interpolate primitive variables instead. Interpolating primitive variables is more robust than interpolating conserved variables since Equation (3.7) is always satisfied. After interpolation, we fill the ghost zones with the conserved variables derived from the interpolated primitive variables. Note that this procedure still preserves conservation because ghost zones do not affect conservation.

*(4) Flux correction operation*

For a leaf coarse patch adjacent to a coarse-fine interface, the flux difference between the coarse and fine patches on the interface will be used to correct the coarse-patch conserved variables adjacent to this interface. If unphysical results are found after this flux correction, we simply ignore the correction on the failed cells. Skipping the correction will break the strict conservation but it only occurs rarely.





# Chapter 4

## Test problems

To understand how evolving the total energy density may deteriorate simulation results and to demonstrate how much the new scheme improves, we compare the results from evolving  $E$  by the flux  $M$  (original scheme) with that from evolving  $\tilde{E}$  by the flux  $(\tilde{E} + p)U_x/\gamma$  (new scheme). Since catastrophic cancellation is likely to occur in UR and NR limits, we will conduct several test problems in these two limits. All simulations throughout this paper adopt the HLLC Riemann solver and PLM data reconstruction unless otherwise specified.

### 4.1 Convergence test for sinusoidal waves

We perturb proper mass density in the high- and low- $T$  limits to compare the accuracy of both schemes over a wide dynamical range. We construct the initial conditions as follows. All cases share homogeneous and static background with proper mass density  $\rho_0 = 1$  on uniform grids, whereas the ambient temperatures are set to  $k_B T/mc^2 = 10^{10}$  and  $10^{-10}$  for the high- and low- $T$  limits, respectively. We then sinusoidally perturb the background with a tiny amplitude,  $\delta\rho/\rho_0 = 10^{-6}$ .

To monitor how errors in the numerical solution decrease as a function of increasing spatial resolution in the three-dimensional space, we adopt a propagating wave along the diagonal direction of the simulation cubic box with the periodic boundary condition. Thus, the analytical solution is  $\rho(\mathbf{x}, t) = \rho_0 + \delta\rho \sin \left[ (x + y + z) / \sqrt{3} - c_s t \right]$ , where  $c_s$  is the sound speed given by Equation (2.14).

We define the L1-norm error as

$$L1(Q) = \frac{1}{N} \sum_{i=1}^N 1 - \frac{Q_{\text{numerical}}(\mathbf{x}_i)}{Q_{\text{analytical}}(\mathbf{x}_i)}, \quad (4.1)$$

where  $Q_{\text{numerical}}(\mathbf{x}_i)$  is the numerical solution of  $i$ -th cell at  $\mathbf{x}_i$  and  $Q_{\text{analytical}}(\mathbf{x}_i)$  is the corresponding analytical solution. We then calculate the L1 error of the proper mass density along the wave propagating direction. As shown in ??, the L1 errors of the new scheme in both the high- $T$  limit (■) and low- $T$  limit (⬢) decrease as  $N^{-2}$ , consistent with the second-order accuracy of the MUSCL-Hancock scheme with PLM data reconstruction. However, the error of the original scheme in the low- $T$  limit (●) is much larger and roughly equal to a constant of  $2 \times 10^{-6}$ . This is expected because the error arising from the original scheme can be estimated from Equation (2.21) in the NR limit:

$$\frac{4}{3 \left( \frac{k_B T}{mc^2} \right)} \epsilon_{\text{machine}}, \quad (4.2)$$

where  $k_B T / mc^2 = 10^{-10}$  and  $\epsilon_{\text{machine}} \sim 10^{-16}$  for double precision.

We thus conclude that for the original scheme in the NR limit, the cancellation between  $(E/Dc^2)^2$  and  $[(\mathbf{M}/Dc)^2 + 1]$  leads to an error of  $\sim 10^{-6}$  when computing primitive variables, roughly consistent with the L1 error (●). For the opposite high- $T$  limit (◆), the discretization error, however, completely overwhelms the error ( $\sim 4\epsilon_{\text{machine}} \sim 4 \times 10^{-16}$ ) estimated from Equation (2.21) in the high- $T$  limit, thus dominating the L1 error. The error arising from the cancellation in the new scheme,  $(\tilde{E}/Dc^2)^2 + 2(\tilde{E}/Dc^2) - (\mathbf{M}/Dc)^2$ , on the left side of Equation (2.15), is close to  $\epsilon_{\text{machine}}$  in both the high- and low- $T$  limits when  $\mathcal{M} < 1$  (see Section 2.3 and Appendix ?? for details).

## 4.2 1-D relativistic Riemann problems

The 1-D Riemann problem [Sod, 1978] has played an important role by providing exact nonlinear solutions against which (relativistic) hydrodynamic codes can be tested. Riemann problem is an initial-value problem with a piece-wise constant initial data that has

Table 4.1: The left and right initial states of the Riemann problems in Section 4.2. We denote the left/right states by the subscript  $L/R$ .

	$p_L$	$\rho_L$	$U_L$	$p_R$	$\rho_R$	$U_R$	Floating-point format
Ultra-relativistic limit	1.0	$10^{-5}$	$10^6$	1.0	$10^{-5}$	$-10^6$	Double precision
Mixed limits	$10^{-4}$	$10^2$	$10^{-3}$	$10^{-10}$	$10^{-12}$	$-10^2$	Single precision

a single discontinuity in the domain of interest. In this section, we directly compare the new and original schemes by simulating two relativistic Riemann problems. We then demonstrate that the new scheme handles both the UR and NR limits very well. By contrast, the original scheme severely suffers from numerical errors in the NR limit. Both schemes share the same numerical setup, e.g., MUSCL-Hancock integration, PLM data reconstruction, hybrid van-Leer, generalized minmod slope limiter, and uniform grids with the outflow boundary condition. In addition, we have numerically derived the exact solution of a nontrivial relativistic Riemann problem with the TM EoS (see Appendix ?? for details) in order to verify the numerical results.

### 4.3 Ultra-relativistic limit

We simulate a head-on collision of two identical gases with  $\gamma = 10^6$  and  $k_B T/mc^2 = 10^5$  with uniform 512 grids. The computational domain is in the interval  $[0, 1]$ . The initial discontinuity is located at  $x = 0.5$ . The first row of Table 4.1 presents the initial right and left states. Figure 4.1 shows the results at  $t = 1.0$ . The left panels show the entire simulation domain, while the right panels show the zoom-in image of the post-shock region, which has been violently heated up to ultra-relativistically hot temperature ( $k_B T/mc^2 \sim 10^{11}$ ) by the extremely high- $\gamma$  gases flowing inwards from both sides. As can be seen, the new scheme (○) fully agrees with the original scheme (✖) on the large-scale profile but also on the small-scale errors, meaning that the new scheme does not sacrifice the numerical accuracy in the UR limit. In addition, we notice that the non-negligible and spurious waves occur in the post-shock region, which are not due to root-finding iterations but to spatial discretization errors as the spurious waves can be reduced by increasing spatial resolution.

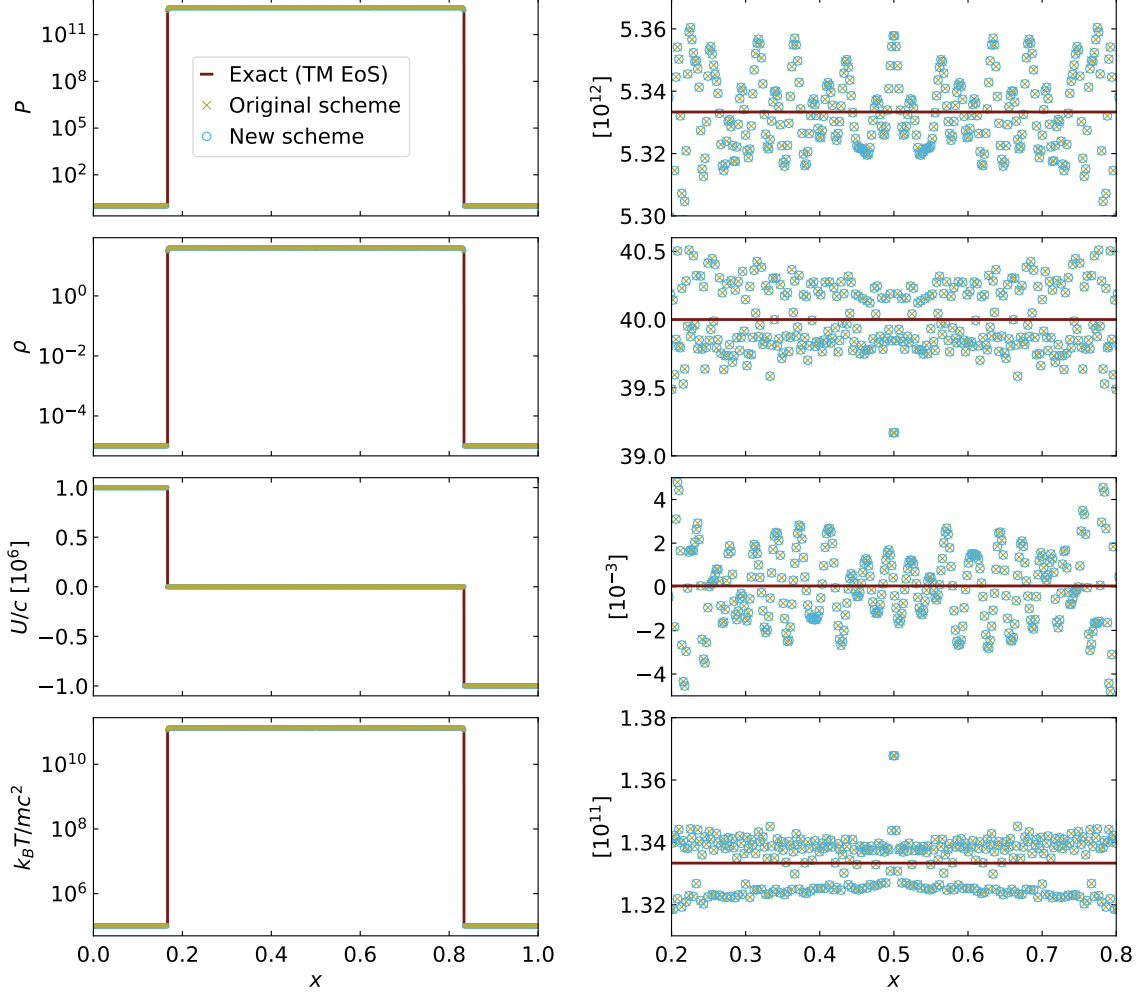


Figure 4.1: Riemann problem in the UR limit with a head-on collision of two identical gases with  $\beta\gamma = 10^6$  and  $k_B T / mc^2 = 10^5$  at  $t = 1.0$ . The left column shows the entire simulation domain, while the right column shows the zoom-in image of the post-shock region. From top to bottom: pressure, proper mass density, four-velocity, and temperature. Note that we plot the Mach number in the zoom-in image (right column) of four-velocity so as to readily compare the amplitude of velocity oscillation with sound speed. The new scheme (blue circles) fully agrees with the original scheme (olive crosses) not only on the large-scale profiles but also on the small-scale errors, meaning that the new scheme (blue circles) does not sacrifice (or improve) the numerical accuracy in the UR limit for that in the NR limit.

## 4.4 Mixed limits

To demonstrate that the new scheme can handle a large dynamical range covering both extremely hot and extremely cold gases, we simulate a nontrivial Riemann problem where the temperature straddles between the high- and low- $T$  limits. This initial condition evolves into a cold left-traveling rarefaction wave separated by a contact discontinuity to match an extremely hot downstream of an ultra-relativistic shock traveling toward the right. Also, we have numerically derived the exact solution of this particular Riemann problem with the TM EoS (see Appendix ??). The second row in Table 4.1 shows the initial left and right states. The simulation adopts a computational domain  $[0,100]$  with 102,400 cells. Since the speed of the right-traveling shock is 276 times faster than that of the left-traveling rarefaction wave, we put the initial discontinuity at  $x = 5 \times 10^{-2}$  to provide an ample space for the right-traveling shock.

Figure 4.2 shows the results at  $t = 80$ , where there are three points to be emphasized. First, we find not only that the shock front at  $x = 26$  is well resolved by 3–4 cells but also that the new scheme (✖) agrees well with the exact solution of the TM EoS (—), as shown in all insets. Second, the L1 error, defined by Equation (4.1), of the density profile from the original scheme (○) is 23 per cent within the region between the head of rarefaction wave ( $x = 2.67 \times 10^{-2}$ , the third number from top in the leftmost column of Table ?? in Appendix ??) and initial discontinuity ( $x = 5 \times 10^{-2}$ ), consistent with the 20 per cent error estimated by Equation (4.2) with  $k_B T/mc^2 = 8 \times 10^{-6}$ . Similar conclusions can be drawn for other physical quantities. However, in the region  $5 \times 10^{-2} < x < 0.3$  swept by the right-traveling contact discontinuity, errors of the original scheme are much larger than the estimate, which requires further investigation. Third, the solutions of the TM EoS (—) match well with both  $\Gamma = 5/3$  (.....) in the NR region ( $x < 0.21$ ) and  $\Gamma = 4/3$  (.....) in the UR region ( $x > 0.27$ ). It demonstrates the capability of capturing the transition from  $\Gamma = 5/3$  (for  $k_B T/mc^2 \rightarrow 0$ ) to  $\Gamma = 4/3$  (for  $k_B T/mc^2 \rightarrow \infty$ ) for the new scheme. The exact solutions of this test are shown in ?? in Appendix ??.

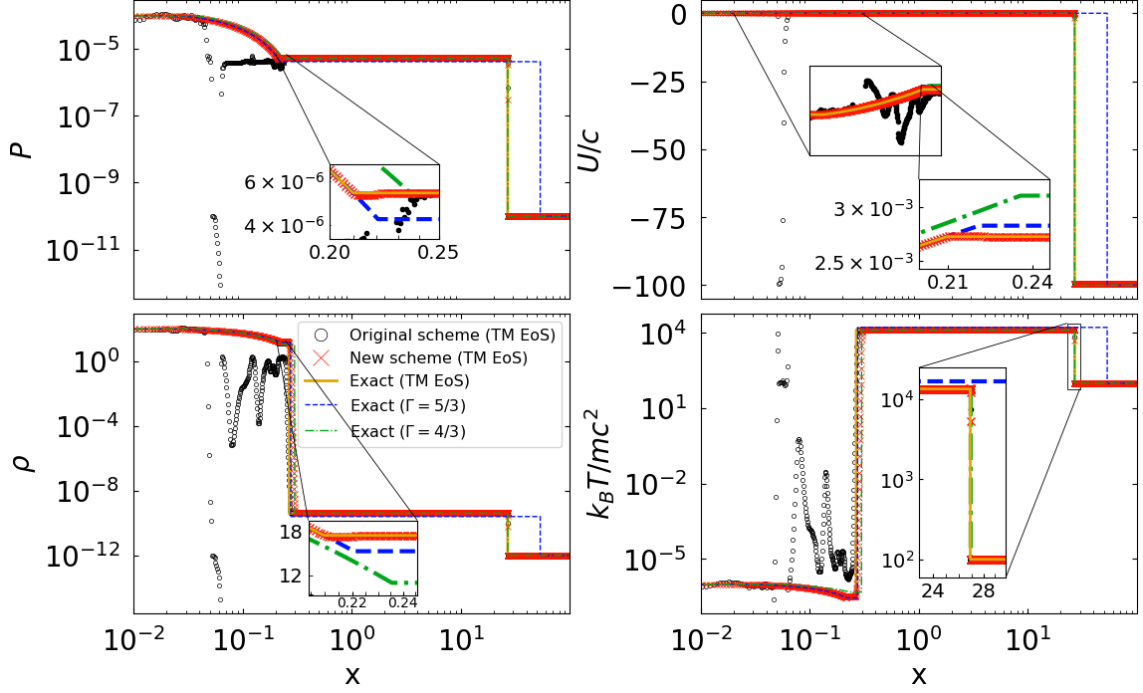


Figure 4.2: Riemann problem in the mixed UR and NR limits at  $t = 80$ . The second row in Table 4.1 shows the initial condition. Clock-wise from top-left: pressure, 4-velocity, temperature, and proper mass density. We find not only that the shock front at  $x = 26$  is well resolved by 3–4 cells but also that the new scheme (red crosses) agrees well with the exact solution of the TM EoS (yellow lines), as shown in all insets. The L1 error of the density profile from the original scheme (black circles) is 23 per cent within the region between the head of rarefaction wave and initial discontinuity (i.e.  $2.67 \times 10^{-2} < x < 5 \times 10^{-2}$ ), consistent with the 20 per cent error estimated by Equation (4.2) with  $k_B T / mc^2 = 8 \times 10^{-6}$ . However, in the region  $5 \times 10^{-2} < x < 0.3$  swept by the right-traveling contact discontinuity, errors of the original scheme are much larger than the estimate, which requires further investigation. The TM profiles match well with both the  $\Gamma = 5/3$  profiles (blue dashed lines) in the NR region ( $x < 0.21$ ) and the  $\Gamma = 4/3$  profiles (green dashed lines) in the UR region ( $x > 0.27$ ).

## 4.5 Multi-dimensional grid effects for high- $\mathcal{M}$ flows

To investigate the detrimental impact of grid effects on the evolution of ultra-relativistic and high Mach number hydrodynamic problems, we separately simulate two identical three-dimensional mono-direction flow with different flow directions. One flow is along the diagonal direction of the simulation box and the other is parallel to the grid direction. Both simulations share the same numerical set-up as follows. Flows are initially represented by cylinders extending to the boundaries of a periodic cubic box with a width  $L$ . The cylinder diameter is  $D = 0.028L$ . The proper mass density ratio of the flow and the ambient is  $\rho_{\text{flow}}/\rho_{\text{amb}} = 10^{-5}$ . The temperatures of the flows and the ambient are  $k_B T_{\text{flow}}/mc^2 = 1.0$  and  $10^{-5}$ , respectively. The four-velocity  $(\gamma\beta)$  profile inside the flow source is  $10^6 (1 + \cos(2\pi r/D))$ , where  $r$  is the distance from the flow axis inside the source. Other physical quantities are uniformly distributed inside the source.

The AMR base level is covered by  $64^3$  cells in all cases. We adopt the gradient of the proper mass density and the magnitude of  $\mathbf{M}/D$  as the two inclusive refinement criteria. We refine a patch if the gradient of a cell satisfies

$$\frac{\Delta h_\ell}{Q} \left( \frac{\partial Q}{\partial x} + \frac{\partial Q}{\partial y} + \frac{\partial Q}{\partial z} \right) > C_Q, \quad (4.3)$$

where  $Q = \rho$ ,  $C_Q = 0.3$ , and  $\Delta h_\ell$  is the cell size at refinement level  $\ell$ . This criterion aims to capture the finger structure due to instabilities at the interface between the flow and the ambient gases. Also, a patch will be refined when any cell satisfies  $\mathbf{M}/D > 10^4$  so that the high-speed region is refined to the finest level.

Figure 4.3 shows the simulation results at  $t = 0.4L/c$ . In Figures 4.3(a) and 4.3(b), we adopt four AMR levels to ensure that the flow diameter can be resolved by 28 cells. The extremely high Mach number ( $\mathcal{M} \sim 10^6$ ) flow leaves any instability short of time to develop, and one expects a smooth flow-ambient interface. However, the interface of the oblique flow turns out to be subject to severe dissipation. The fuzzy-looking cross-sections in the transverse slices of the oblique flow (right column in Figure 4.3(b)) suggest that the dissipation is caused by numerical instabilities when high Mach number flow travels

obliquely across Cartesian grids. This numerical problem is not limited to relativistic high Mach number flows but also occurs in non-relativistic high Mach number flows.

To examine this issue further, we increase the spatial resolution by a factor of 2 and decrease the time-step by a factor of 0.3 from the standard Courant condition. The results (Figures 4.3(c) and 4.3(d)) indicate that increasing spatial and temporal resolution can neither significantly ameliorate the dissipation nor help the oblique flow converge to the horizontal flow. This artificial grid effect can adversely influence the study of high-speed jets, especially for hydrodynamical instabilities near the jet boundaries.

An example of this boundary instability is the finger-like pattern observed immediately outside the parallel flow (right column in Figure 4.3(a)), which we believe to arise from a genuine instability seeded by discretization noise. The finger-like pattern has a higher temperature than the ambient, and in fact consists of two-dimensional flat sheets along the flow. This is demonstrated in Figure 4.4 with transverse slices cut through ‘B’ and ‘C’. The patterns are identical to that cut through ‘A’ in Figure 4.3(c). These 2-D sheet pattern persists even after adding 1 per cent level of white noise into the background density, illustrating that the coherence of sheets along the flow direction is genuinely generated by the high-speed flow boundaries. This finger pattern is similar, but not identical, to the curvature-driven fingers of a knotted jets reported recently [Gourgouliatos and Komissarov, 2017]. Our flow has a smooth and parallel boundary without any curvature to drive the fingers.



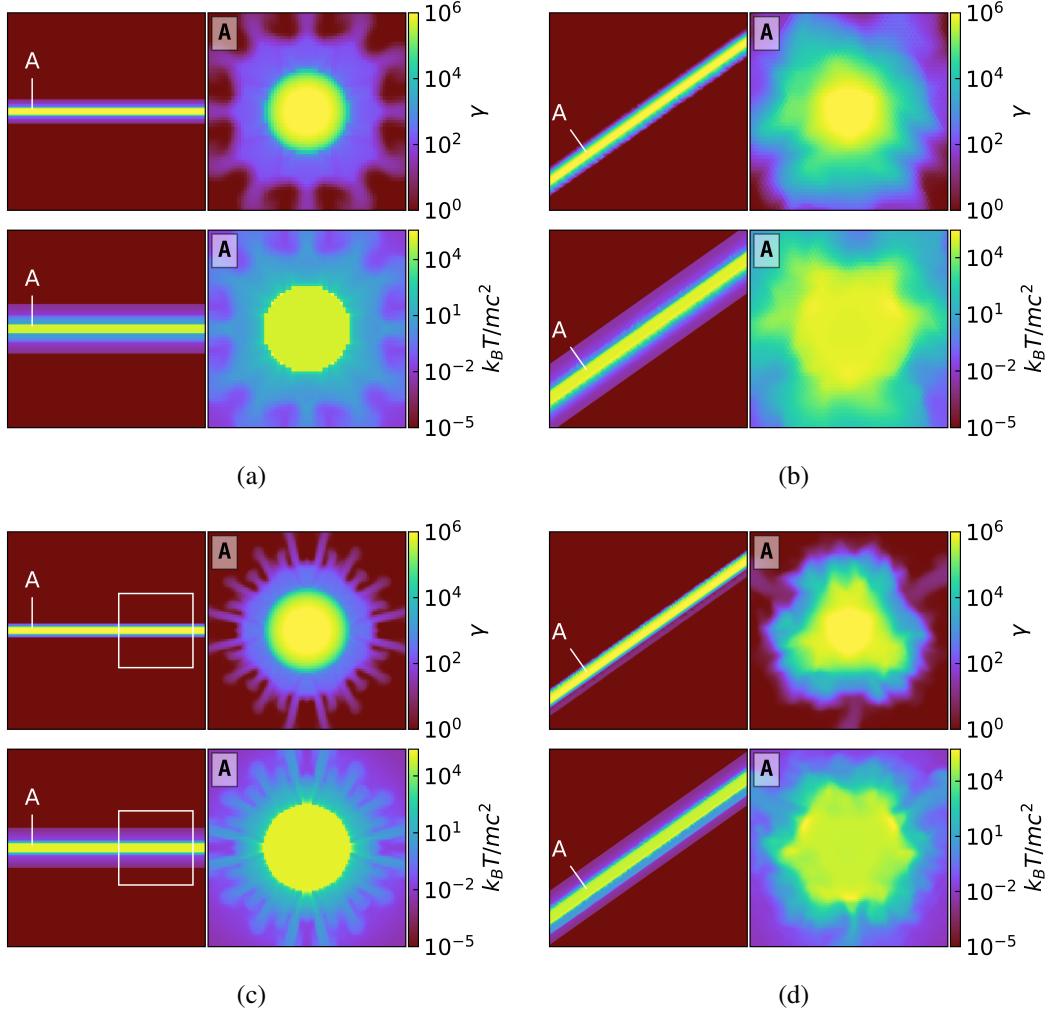


Figure 4.3: Ultra-relativistic flows propagating along different spatial directions with respect to the grids. In all subfigures (a)–(d), the left and right columns are the longitudinal and transverse slices, respectively. Longitudinal slices are taken through the flow source while the transverse slices are taken through the label ‘A’. The flow diameter is resolved by 28 cells in (a) and (b) and by 56 cells in (c) and (d). The flow has an extremely high Mach number ( $\mathcal{M} \sim 10^6$ ) leaving any instability short of time to develop, and one expects a smooth flow-ambient interface. However, the fuzzy-looking cross-sections in the transverse slices of the oblique flow (right columns in (b) and (d)) suggest that the high-speed flow induces false instability when the flow travels obliquely across Cartesian grids. Increasing the spatial and temporal resolution does not help the numerical solution of an oblique flow to converge to that of a parallel flow.

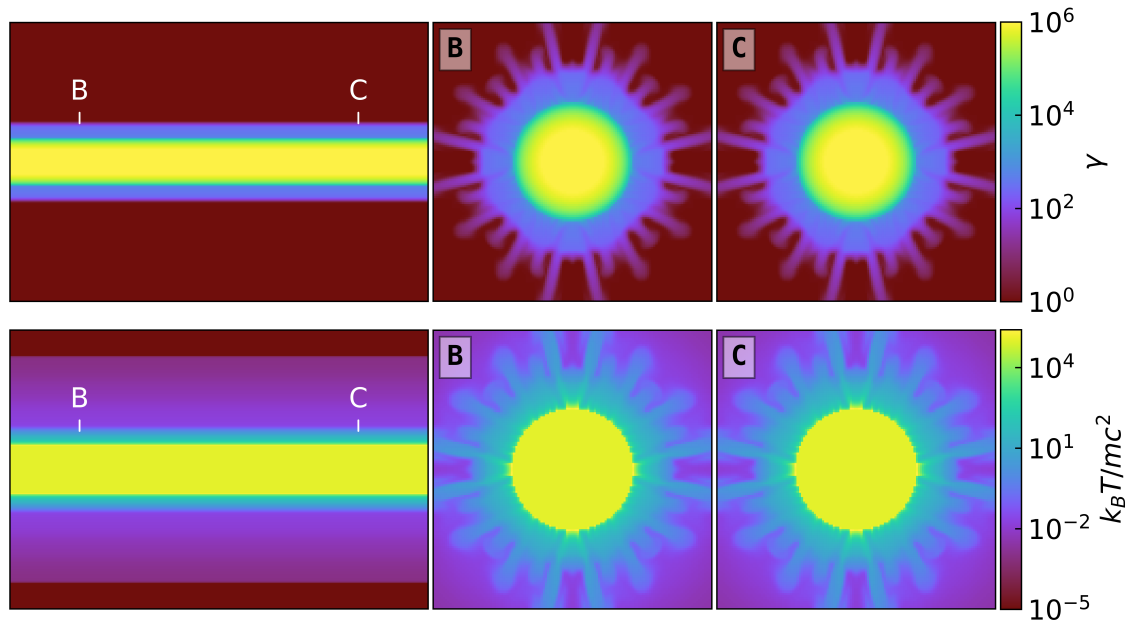


Figure 4.4: Close-up view of the rectangular region in Figure 4.3(c) with longitudinal (first column from the left) and transverse (other columns) slices passing through 'B' and 'C', respectively. Compared with Figure 4.3(c), it clearly shows that the finger pattern consists of 2-D flat sheets along the flow.

# Bibliography

- R. Blandford, D. Meier, and A. Readhead. Relativistic jets from active galactic nuclei. *Annual Review of Astronomy and Astrophysics*, 57(1):467–509, 2019. . URL <https://doi.org/10.1146/annurev-astro-081817-051948>.
- T. Chiueh. Relativistic solitons and shocks in magnetized  $e^-e^+p^+$  fluids. *Phys. Rev. Lett.*, 63:113–116, Jul 1989. . URL <https://link.aps.org/doi/10.1103/PhysRevLett.63.113>.
- T. Chiueh, Z.-Y. Li, and M. C. Begelman. Asymptotic Structure of Hydromagnetically Driven Relativistic Winds. , 377:462, Aug. 1991. .
- T. Chiueh, Z.-Y. Li, and M. C. Begelman. A critical analysis of ideal magnetohydrodynamic models for crab-like pulsar winds. *The Astrophysical Journal*, 505(2):835–843, oct 1998. . URL <https://doi.org/10.1086%2F306209>.
- S. A. E. G. Falle. Self-similar jets. *Monthly Notices of the Royal Astronomical Society*, 250(3):581–596, 06 1991. ISSN 0035-8711. . URL <https://doi.org/10.1093/mnras/250.3.581>.
- W. Fong, P. K. Blanchard, K. D. Alexander, J. Strader, R. Margutti, A. Hajela, V. A. Villar, Y. Wu, C. S. Ye, E. Berger, R. Chornock, D. Coppejans, P. S. Cowperthwaite, T. Eftekhari, D. Giannios, C. Guidorzi, A. Kathirgamaraju, T. Laskar, A. Macfadyen, B. D. Metzger, M. Nicholl, K. Paterson, G. Terreran, D. J. Sand, L. Sironi, P. K. G. Williams, X. Xie, and J. Zrake. The Optical Afterglow of GW170817: An Off-axis Structured Jet and Deep Constraints on a Globular Cluster Origin. , 883(1):L1, Sept. 2019. .

- B. Fryxell, K. Olson, P. Ricker, F. X. Timmes, M. Zingale, D. Q. Lamb, P. MacNeice, R. Rosner, J. W. Truran, and H. Tufo. FLASH: An adaptive mesh hydrodynamics code for modeling astrophysical thermonuclear flashes. *The Astrophysical Journal Supplement Series*, 131(1):273–334, nov 2000. . URL <https://doi.org/10.1086%2F317361>.
- G. Ghirlanda, O. S. Salafia, Z. Paragi, M. Giroletti, J. Yang, B. Marcote, J. Blanchard, I. Agudo, T. An, M. G. Bernardini, R. Beswick, M. Branchesi, S. Campana, C. Casadio, E. Chassande-Mottin, M. Colpi, S. Covino, P. D’Avanzo, V. D’Elia, S. Frey, M. Gawronski, G. Ghisellini, L. I. Gurvits, P. G. Jonker, H. J. van Langevelde, A. Melandri, J. Moldon, L. Nava, A. Perego, M. A. Perez-Torres, C. Reynolds, R. Salvaterra, G. Tagliaferri, T. Venturi, S. D. Vergani, and M. Zhang. Compact radio emission indicates a structured jet was produced by a binary neutron star merger. *Science*, 363(6430):968–971, Mar. 2019. .
- K. N. Gourgouliatos and S. S. Komissarov. Reconfinement and loss of stability in jets from active galactic nuclei. *Nature Astronomy*, 2(2):167–171, Dec. 2017. . URL <https://doi.org/10.1038/s41550-017-0338-3>.
- N. J. Higham. *Accuracy and Stability of Numerical Algorithms*. Society for Industrial and Applied Mathematics, USA, 2nd edition, 2002. ISBN 0898715210.
- F. Jüttner. Das maxwellsche gesetz der geschwindigkeitsverteilung in der relativtheorie. *Annalen der Physik*, 339(5):856–882, 1911. . URL <https://onlinelibrary.wiley.com/doi/abs/10.1002/andp.19113390503>.
- C. F. Kennel and F. V. Coroniti. Confinement of the Crab pulsar’s wind by its supernova remnant. , 283:694–709, Aug. 1984a. .
- C. F. Kennel and F. V. Coroniti. Magnetohydrodynamic model of Crab nebula radiation. , 283:710–730, Aug. 1984b. .
- Z.-Y. Li, T. Chiueh, and M. C. Begelman. Electromagnetically Driven Relativistic Jets: A Class of Self-similar Solutions. , 394:459, Aug. 1992. .

F. D. Lora-Clavijo, A. Cruz-Osorio, and F. S. Guzmán. CAFE: A NEW RELATIVISTIC MHD CODE. *The Astrophysical Journal Supplement Series*, 218(2):24, jun 2015. . URL <https://doi.org/10.1088%2F0067-0049%2F218%2F2%2F24>.

W. G. Mathews. The Hydromagnetic Free Expansion of a Relativistic Gas. , 165:147, Apr 1971. .

A. Mignone and G. Bodo. An HLLC Riemann solver for relativistic flows —I. Hydrodynamics. *Monthly Notices of the Royal Astronomical Society*, 364(1):126–136, 11 2005. ISSN 0035-8711. . URL <https://doi.org/10.1111/j.1365-2966.2005.09546.x>.

A. Mignone and G. Bodo. An HLLC Riemann solver for relativistic flows –II. Magnetohydrodynamics. *Monthly Notices of the Royal Astronomical Society*, 368(3):1040–1054, 04 2006. ISSN 0035-8711. . URL <https://doi.org/10.1111/j.1365-2966.2006.10162.x>.

A. Mignone and J. C. McKinney. Equation of state in relativistic magnetohydrodynamics: variable versus constant adiabatic index. *Monthly Notices of the Royal Astronomical Society*, 378(3):1118–1130, 06 2007. ISSN 0035-8711. . URL <https://doi.org/10.1111/j.1365-2966.2007.11849.x>.

A. Mignone, T. Plewa, and G. Bodo. The piecewise parabolic method for multidimensional relativistic fluid dynamics. *The Astrophysical Journal Supplement Series*, 160, 09 2005. .

K. P. Mooley, A. T. Deller, O. Gottlieb, E. Nakar, G. Hallinan, S. Bourke, D. A. Frail, A. Horesh, A. Corsi, and K. Hotokezaka. Superluminal motion of a relativistic jet in the neutron-star merger GW170817. , 561(7723):355–359, Sept. 2018a. .

K. P. Mooley, E. Nakar, K. Hotokezaka, G. Hallinan, A. Corsi, D. A. Frail, A. Horesh, T. Murphy, E. Lenc, D. L. Kaplan, K. de, D. Dobie, P. Chand ra, A. Deller, O. Gottlieb, M. M. Kasliwal, S. R. Kulkarni, S. T. Myers, S. Nissanke, T. Piran, C. Lynch,

- V. Bhalerao, S. Bourke, K. W. Bannister, and L. P. Singer. A mildly relativistic wide-angle outflow in the neutron-star merger event GW170817. , 554(7691):207–210, Feb. 2018b. .
- S. C. Noble, C. F. Gammie, J. C. McKinney, and L. D. Zanna. Primitive variable solvers for conservative general relativistic magnetohydrodynamics. *The Astrophysical Journal*, 641(1):626–637, apr 2006. . URL <https://doi.org/10.1086%2F500349>.
- J. Núñez-de la Rosa and C.-D. Munz. XTROEM-FV: a new code for computational astrophysics based on very high order finite-volume methods - II. Relativistic hydro- and magnetohydrodynamics. , 460(1):535–559, Jul 2016. .
- D. Ryu, I. Chattopadhyay, and E. Choi. Equation of state in numerical relativistic hydrodynamics. *The Astrophysical Journal Supplement Series*, 166(1):410–420, sep 2006. . URL <https://doi.org/10.1086%2F505937>.
- H.-Y. Schive, Y.-C. Tsai, and T. Chiueh. GAMER: A GRAPHIC PROCESSING UNIT ACCELERATED ADAPTIVE-MESH-REFINEMENT CODE FOR ASTROPHYSICS. *The Astrophysical Journal Supplement Series*, 186(2):457–484, feb 2010. . URL <https://doi.org/10.1088%2F0067-0049%2F186%2F2%2F457>.
- H.-Y. Schive, J. A. ZuHone, N. J. Goldbaum, M. J. Turk, M. Gaspari, and C.-Y. Cheng. gamer-2: a GPU-accelerated adaptive mesh refinement code –accuracy, performance, and scalability. *Monthly Notices of the Royal Astronomical Society*, 481(4):4815–4840, 09 2018. ISSN 0035-8711. . URL <https://doi.org/10.1093/mnras/sty2586>.
- G. A. Sod. A survey of several finite difference methods for systems of nonlinear hyperbolic conservation laws. *Journal of Computational Physics*, 27(1):1 – 31, 1978. ISSN 0021-9991. . URL <http://www.sciencedirect.com/science/article/pii/0021999178900232>.
- J. L. Synge. The Relativistic Gas. *North-Holland Pub. Co.; Interscience Publishers*, 1957.
- A. H. Taub. Relativistic Rankine-Hugoniot Equations. *Physical Review*, 74(3):328–334, Aug 1948. .

- E. F. Toro. *Riemann solvers and numerical methods for fluid dynamics : a practical introduction*. Springer, Berlin, 2011.
- M. J. Turk, B. D. Smith, J. S. Oishi, S. Skory, S. W. Skillman, T. Abel, and M. L. Norman. yt: A Multi-code Analysis Toolkit for Astrophysical Simulation Data. *The Astrophysical Journal Supplement Series*, 192:9, Jan. 2011. .
- B. van Leer. Towards the ultimate conservative difference scheme. v. a second-order sequel to godunov's method. *Journal of Computational Physics*, 32(1):101–136, jul 1979. . URL [https://doi.org/10.1016/0021-9991\(84\)90145-1](https://doi.org/10.1016/0021-9991(84)90145-1).
- B. van Leer. Upwind and high-resolution methods for compressible flow: From donor cell to residu volume = 1, journal = Communications in Computational Physics. pages 192–206, 04 2006.
- P. Woodward and P. Colella. The numerical simulation of two-dimensional fluid flow with strong shocks. *Journal of Computational Physics*, 54(1):115–173, Apr. 1984. . URL [https://doi.org/10.1016/0021-9991\(84\)90142-6](https://doi.org/10.1016/0021-9991(84)90142-6).
- S. E. Woosley. Gamma-Ray Bursts from Stellar Mass Accretion Disks around Black Holes. , 405:273, Mar. 1993. .